Majorana zero modes in a cylindrical semiconductor quantum wire

Chao Lei, Guru Khalsa, Jiangfeng Du, and Allan H. MacDonald

Phys. Rev. B **104**, 035426 — Published 21 July 2021

DOI: 10.1103/PhysRevB.104.035426

Majorana Zero Modes in Cylindrical Semiconductor Quantum Wire

Chao Lei,[1,2] Guru Khalsa,[2,3] Jiangfeng Du,[1] and Allan H. MacDonald[2]

[1] *Department of Modern Physics, University of Science and Technology of China, Hefei, Anhui 230026, China*
[2] *Department of Physics, The University of Texas at Austin, Austin, Texas 78712,USA*
[3] *Department of Materials Science and Engineering, Cornell University, Ithaca, New York 14853, USA*

We study Majorana zero modes properties in cylindrical cross-section semiconductor quantum wires based on the effective-mass theory and a discretized lattice model. Within this model the influence of disordered potentials in the quantum wire as well as amplitude and phase fluctuations of the superconducting order-parameter are discussed. We find that for typical wire geometries, pairing potentials, and spin-orbit coupling strengths, coupling between quasi-one-dimensional sub-bands is weak, low-energy quasiparticles near the Fermi energy are nearly completely spin-polarized, and the number of electrons in the active sub-bands of topological states is less than ten.

I. INTRODUCTION

One-dimensional (1D) p-wave superconductors are topologically nontrivial[1] and, in finite systems, support end-localized Majorana zero modes.[2] These states have attracted considerable interest lately[3–9] because of their non-Abelian exchange properties,[10,11] and related potential utility in quantum information processing systems[3]. Theory has suggested[12,13] that it should be possible to engineer effective one-dimensional p-wave superconductors in proximity coupled semiconductor quantum wires by combining broken inversion symmetry, and the consequent Rashba spin-orbit interactions, with external magnetic fields. Considerable progress has been made in exploring this idea experimentally.[14–44] There has also been progressed toward Majorana-based quantum state manipulation in other systems, including magnetic atom chains,[45–47] interfaces between conventional superconductors and topological insulators,[48,49] iron-based superconductors,[50] and phase-controlled Josephson junctions.[51,52]

The Majorana zero modes in semiconductor quantum wires[53–56] are expected to appear only when external magnetic field strengths exceed a critical value, beyond which the proximity-induced superconductor gap vanishes. Early experiments in cylindrical cross section quantum wires exhibit many trends consistent with expectations[14–19] based on Majorana zero mode properties, although they also consistently exhibit evidence of a soft gap, *i.e.* of quasiparticle states within the gap, at all magnetic field strengths. The in-gap states can be associated with spatially extended Andreev states,[57] disorder[58–60] or Kondo effects,[61] and may influence electron transport experiments, and thus would poison any attempt to achieve topologically protected state manipulation.

In this paper, we study quasi-one-dimensional cylindrical quantum wires numerically (A main reason is that in experiments, the longest quantum wires have approximate cylindrical cross-sections, longer wires have weaker hybridization between Majorana zero modes at the ends of quantum wire, and more electrons inactive sub-bands.), using experimentally realistic geometries diameters $\sim$ 100 nm, as shown in Fig. 1, experimentally estimated pairing potential and spin-orbit coupling strengths, and a variety of types of experimentally realistic disorder.

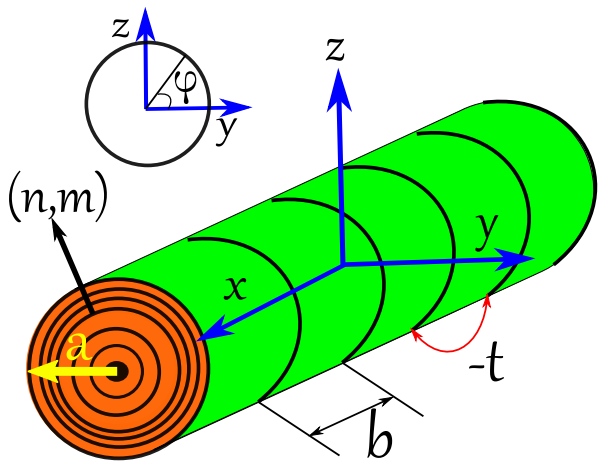

FIG. 1. (Color online). Cylindrical semiconductor quantum wire geometry. Here a labels the radius of the cylindrical quantum wire, b is the lattice constant used to discretize position along the wire in our numerical studies, and t the corresponding hopping strength. The circles in the cross-section schematically represent radial wavefunctions labeled by principal axial quantum number n and angular momentum m.

The remaining of our paper is organized as follows. In Section II we introduce a theoretical model for cylindrical quantum wires and discuss its topological-state phase diagram as a function of Fermi energies and magnetic fields. In Section III we analyze the Andreev states, and the tunneling density of states as a function of magnetic fields, disordered potential, and pairing-potential(or phase) disorder in infinite quantum wires. In Section IV we address the case of finite quantum wire with lengths on the scale of experimental samples, discuss the effects of finite-length Majorana energy splitting and disorder. In Section V we discuss the use of models in which only degrees of freedom in the semiconductor quantum wire

are included, *vs.* models that account explicitly for the superconducting metal.

II. EFFECTIVE-MASS THEORY

When Rashba spin-orbit interactions are neglected, the cylindrical-coordinate effective-mass theory Hamiltonian for an n-type semiconductor quantum wire oriented along the $\hat{x}$ direction (shown in Fig. 1) separates into a free-particle contribution along the wire and a radial confinement contribution.[62,63] The Hamiltonian is

$$\mathcal{H}_0 = \frac{\hbar^2}{2m^*}(k_x^2 - \frac{\partial^2}{\partial r^2} - \frac{1}{r}\frac{\partial}{\partial r} - \frac{1}{r^2}\frac{\partial^2}{\partial \varphi^2}) + V(\mathbf{r}, x) \quad (1)$$

where $\hbar$ is Planck's constant, m^* is the conduction band effective mass, $V(\mathbf{r}, x)$ is the confining potential, $\mathbf{r} = (y, z) = (r\cos(\varphi), r\sin(\varphi))$ is the position projected to the wire cross-section, x is position along the wire, and k_x is wave vector along the wire. In the absence of disorder, we take $V(\mathbf{r}, x)$ to be 0 inside the wire ($|\mathbf{r}| < a$ where a the radius of the wire) and $+\infty$ outside the wire.

Cylindrical symmetry implies that eigenstates can be labeled by angular momentum m along the wire axis. The confined radial wave functions are then Bessel functions with zeros at the wire edge. The one-dimensional transverse wave-functions are

$$f_{n,m}(r, \varphi) = \; A_{n,m} J_{|m|}(u_{n,m}\tfrac{r}{a})\, e^{im\varphi}, \;\; m = 0, \pm 1, \pm 2, ... \quad (2)$$

where $J_{|m|}(u_{n,m}\frac{r}{a})$ is an $m^{th}-$order Bessel function, $u_{n,m}$ is the n^{th} zero of the m^{th}-order Bessel function, and $A_{n,m} = 1/[a\sqrt{\pi}J_{|m|+1}(u_{n,m})]$ is a normalization constant. The one-dimensional sub-bands are rigidly offset by an energy which is determined by the principal axial quantum number n and the azimuthal quantum number m that quantifies the angular momentum. The dispersion is

$$E_{n,m}(k_x) = \frac{\hbar^2}{2m^*}k_x^2 + \frac{\hbar^2}{2m^*}\frac{u_{n,m}^2}{a^2}. \quad (3)$$

Note that since $u_{n,m} = u_{n,-m}$, so $|m| \neq 0$ sub-bands are always doubly degenerate.

The mean-field Hamiltonian of a spin-orbit coupled quantum wire with proximity-induced s-wave superconductivity and an external magnetic field includes one-dimensional sub-band, Rashba, Zeeman, and pairing contributions:

$$\mathcal{H} = \mathcal{H}_0 + \mathcal{H}_R + \mathcal{H}_Z + \mathcal{H}_{SC}. \quad (4)$$

It is convenient to express this Hamiltonian in the representation of parabolic band quantum wire eigenstates. Assuming that the quantum wire is placed on a substrate with a $\hat{z}$ direction surface normal, the quantum wire Rashba Hamiltonian is

$$\mathcal{H}_R = \alpha\left[-i(\sin\varphi\frac{\partial}{\partial r} + \frac{\cos\varphi}{r}\frac{\partial}{\partial \varphi})\sigma_x - k_x\sigma_y\right], \quad (5)$$

where α is the Rashba coupling parameter and σ_α is a Pauli matrix acting on spin. Note that although the radial and angular momentum operators are not Hermitian in cylindrical coordinate, the sum of them is in fact Hermitian as we show in Appendix B. The matrix elements of the Rashba Hamiltonian in the representation of unperturbed band states are

$$\langle n, m|\mathcal{H}_R|n', m'\rangle = -i\alpha k_x\sigma_y\delta_{n,n'}\delta_{m,m'} - \alpha R_{nm;n'm'}\sigma_x, \quad (6)$$

where

$$R_{nmn'm'} = \langle f_{nm}|\,(\sin\varphi\frac{\partial}{\partial r} + \frac{\cos\varphi}{r}\frac{\partial}{\partial\varphi})\,|f_{n'm'}\rangle \quad (7)$$

is non-zero for $m = m' \pm 1$.

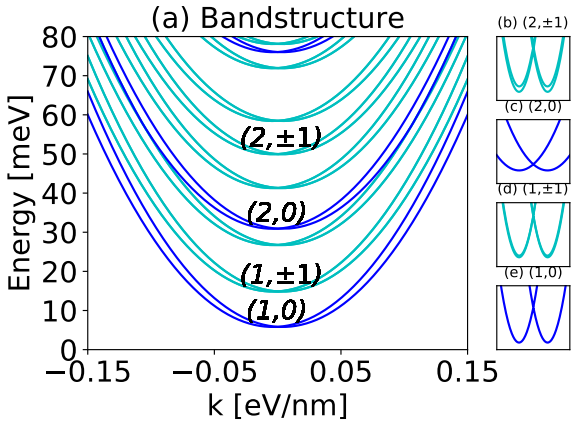

FIG. 2. (Color online). One-dimensional band-structure of a cylindrical semiconductor quantum wire with radius $a = 50$nm, InSb conduction band mass $m^* = 0.015m_e$, and Rashba coupling parameter $\alpha = 0.02$ eV $\cdot$ nm. The panels on the right highlight the behaviors near band minima, which are important for topological superconductivity.

The one-dimensional band structure with quantum numbers labeled by (n,m) is illustrated in Fig. 2. These results were obtained by using parameters that are appropriate for the $a = 50$ nm InSb quantum wire ($m^* = 0.015m_e$) studied in the first Majorana experiment[14] with Rashba coupling parameter $\alpha = 0.02$ eV $\cdot$ nm. We note that subsequent experiments studied quantum wires with similar properties. Angular momentum m is not a good quantum number for finite Rashba coupling strength. Because the Rashba interaction couples only states that differ by ± 1 in angular momentum, the mixing between $m + 1$ and $m - 1$ sub-bands is second-order in the ratio of the Rashba coupling strength ($\sim \alpha/a$) to the sub-band separations, which is small and lift the $\pm m$ degeneracy (as shown in Fig. 2) at finite k_x, and lift the spin-degeneracy within each sub-band.

In quantum wires with a radius of $a = 50$ nm, magnetic orbital effects are inevitably present when the magnetic field is along the quantum wire. The Hamiltonian arising

from the orbital effect is:[63]

$$\mathcal{H}_{orb} = \frac{\hbar^2}{2m^*}\frac{1}{l_x^2}\frac{\partial}{\partial\varphi}, \tag{8}$$

where $l_x = \sqrt{\hbar c/eB_x}$ is the magnetic length. This orbital contribution lifts the degeneracy of the subbands with $\pm m$, leading to an energy difference of $m\hbar^2/m^*l_x^2$ which depends on the angular quantum number and the strength of the magnetic field. Note that the magnetic orbital effect has no influence on subbands with angular quantum number $m = 0$. According to the experimental parameters, the critical magnetic field can lift the degeneracy of subband $m = \pm 1$ by around 1 meV (This magnetic orbital effect was also found to be related with the observed large g factor in semiconductor quantum wire.[64]). The Zeeman Hamiltonian can be written as:

$$\mathcal{H}_Z = \mathbf{B}\cdot\boldsymbol{\sigma}, \tag{9}$$

where $\mathbf{B}$ is the magnetic field expressed in energy units. In most experiments the magnetic field is along the $\hat{x}$ direction. The proximity-induced s-wave pairing contribution to the Hamiltonian is

$$\mathcal{H}_{SC} = \sum_{n,m}\left[\Delta_{SC}^* c_{nm\downarrow k}^\dagger c_{nm\uparrow -k}^\dagger + \Delta_{SC} c_{nm\uparrow -k} c_{nm\downarrow k}\right], \tag{10}$$

where $\Delta_{SC} = |\Delta_{SC}|e^{i\phi}$ is the proximity induced gap. The value of Δ_{SC} depends on a complex hybridization processes between orbitals in the quantum wire and orbitals in the surrounding superconductor but can be fit to experimental observations. The relatively large values of Δ_{SC} (0.25 meV in Ref. 14 for example) suggest that the interface between the quantum wire and the surrounding superconductor is quite transparent. We will return to his point in the discussion section.

Topologically distinct phases are separated in coupling-constant parameter space by gapless boundary states. In the case of topological superconductivity in quantum wires, the coupling constants that are readily varied in experiments are the position of the Fermi level relative to the conduction band minimum, which can be altered by manipulating gate voltages, and the strength of the magnetic field responsible for Zeeman coupling to the spin degree of freedom. In the absence of an external magnetic field all states are topologically trivial. As the magnetic field strength increases, the energy gap produced by the proximity effect pairing potential closes at critical field. The phase diagram in Fig. 3 was constructed by tracking these band closings and identifying each with a phase transition from a topologically trivial to a nontrivial state. While increasing the magnetic field with the Fermi level positioned near a sub-band, the superconductor gap closes when the system is driven from trivial superconductivity to non-trivial topological superconductivity. The phase diagram is got by tuning the Fermi level and magnetic field (shown as Fig. 3).

When the Zeeman Energy exceeds the pairing potential, a Majorana zero mode appears while the Fermi level is tuned to lie at the bottom of a non-degenerate subbands. Pairs of localized zero modes appear at each end near the population thresholds of degenerated subbands, they are not really Majorana zeros modes as at each end of quantum wires as there are two or more zero modes, which we called Majorana-like zero modes. These states survive in quantum wires with small cross-section in which the magnetic orbital effect is negligible. For quantum wires with large cross section, the degeneracy of the subbands is lifted by magnetic orbital effect, and thus these states are back to Majorana zero modes.

For sub-bands $n = 1, 2$ and $m = 0, \pm 1$ (see Fig.3), these six sub-bands have the Fermi energy of $E_{F1} \approx 5.87$ meV, $E_{F2} \approx E_{F3} \approx 14.9$ meV, $E_{F4} \approx 30.96$ meV and $E_{F5} \approx E_{F6} \approx 50$ meV. In the phase diagram we use Roman numerals to label the number of Majorana (or Majorana-like if there are more than 2 modes) end-localized states (I – one localized state, II – two localized states, etc.). The bottom panel of Fig. 3 shows the phase diagram for small Zeeman energy where we note that more detail can be seen. Due to the lack of degeneracy of the sub-bands in Fig. 3(b,d) we expect robust Majorana modes, but in Fig. 3(c,e) where sub-bands are nearly degenerate, we expect Majorana-like modes that are weakly coupled. When magnetic orbital effects are considered, this degeneracy is lifted for subbands with non-zero angular quantum numbers. In this case the phase diagrams are shown in Fig. 3 (f)-(i), where the Majorana-like states disappear. In contrast to the $m = 0$ subband, the phase boundary of the $m = \pm 1$ subbands now depends sensitively on the magnetic field strength. The linear dependence of subband splitting with the magnetic field through the magnetic orbital effect subtly adjusts the chemical potential in order to maintain the topological phase. In what follows we will ignore the magnetic orbital effect when calculating the properties of Majorana zero modes for convenience in numerical evaluation.

III. ANDREEV STATES

In contrast to the Majorana modes, zero-bias conductance peaks (ZBCP) in transport experiments may also come from Andreev states which were recently studied experimentally.[21] Here we distinguish between the evolution of Andreev states and Majorana zero modes by varying the magnetic field. From the discussion of Section II, we see that there are degenerate sub-bands which are weakly coupled by Rashba interactions for non-zero angular momentum, while the zero-angular momentum sub-bands are not degenerate. To find the energy spectrum for finite wires we use a quantization and discretization scheme that takes $k_x \to -i\partial/\partial x$ and $\partial^2 c(x)/\partial x^2 \approx (c_{i+1} + c_{i-1} - 2c_i)/b^2$ and $\partial c(x)/\partial x \approx (c_{i+1} - c_{i-1})/2b$, where b is the effective lattice constant shown in Fig. 1.

With periodic boundary condition, i.e. $c_{N+1} = c_1$, there is no Majorana zero mode, and only Andreev states appear as shown in Fig. 4, where we set the length of

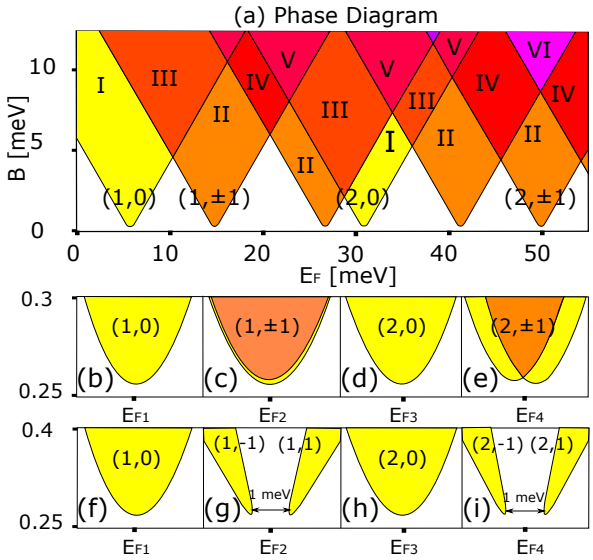

FIG. 3. (Color online). Phase diagram of the cylindrical semiconductor quantum wire as a function of Fermi level and magnetic field. (a) At each sub-band there appears Majorana(-like) zero-modes when the magnetic field exceeds the pairing potential and the Fermi level is tuned to the bottom of the sub-bands, of which n = 1,2 and m = $0, \pm 1$ sub-bands have the Fermi energy at $E_{F1} \approx 5.87$ meV, $E_{F2} \approx E_{F3} \approx 14.9$ meV, $E_{F4} \approx 30.96$ meV and $E_{F5} \approx E_{F6} \approx 50$ meV. In the figure we use Roman numerals and color coordination to label the number of Majorana-like end-localized states. (b-e) Phase diagram focused near the band minima for different (n,m). (f-i) are phase diagrams when magnetic orbit effects are considered.

quantum wire to be 1 μm. We find that numerical convergence in the spectrum of the quantum wire Majorana and Andreev states begins when b is less than 100 nm. We have chosen a stringent convergence condition of $b =$ 5 nm throughout the manuscript to also account for converged bulk states. (See Appendix A for more details.)

In Fig. 4 (a)-(c) we show the density of states (DOS) of the sub-bands with quantum number of (n,m)=(1,0),(1,±1) and (2,0). The DOS is calculated via the following definition:

$$\mathcal{D}(E) = \sum_{n=1}^{\infty} \delta(E - E_n). \tag{11}$$

In the numerical calculations, $\delta(E - E_n)$ is replaced by a Gaussian smearing funcion:

$$g(E - E_n) = \frac{1}{\sqrt{2\pi} w} e^{-\frac{(E-E_n)^2}{2w^2}}, \tag{12}$$

in which w is that width of the smearing. In our calculations w is set to 0.02 meV. We reiterate that the sub-bands with quantum number (1,±1) are weakly coupled through coupling to other sub-bands, as previously discussed. The DOS when the Fermi level is tuned at the bottom of the lowest sub-band (that with quantum number of (n,m)=(1,0)) is shown in Fig. 4 (a), with the Zeeman energy varying from 0 to $4\Delta_{SC}$. The edges of the superconducting gap are labeled with red arrows. When the magnetic field increases, a pair of Andreev states cross when the Zeeman energy equals the pairing potential. Similar crossings happen for $(n, m) = (1, \pm 1)$ and $(n, m) = (2, 0)$ sub-bands. When the periodic boundary condition is removed, i.e. for finite length quantum wires, this pair of Andreev states evolve into Majorana zero-modes, which remain at zero energy once the Zeeman energy exceeds the pairing potential as in Fig. 4 (d).

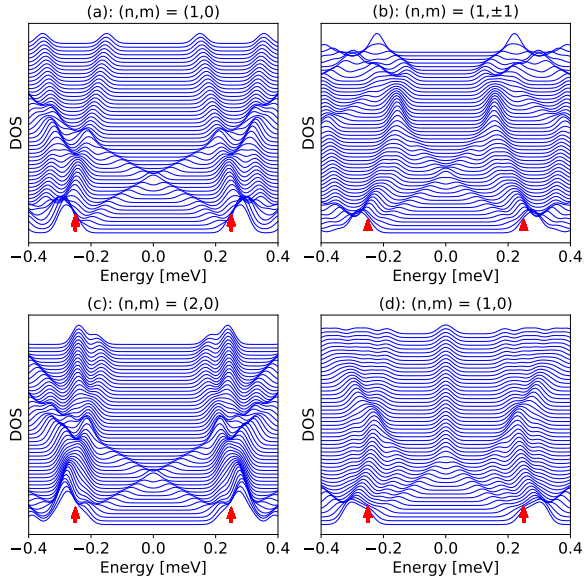

FIG. 4. (Color online). Evolution of Andreev states and Majorana zero modes *vs.* magnetic field. (a)-(c) show the DOS of the infinite wire when the Fermi level is tuned at the bottom of sub-bands with different quantum numbers. The magnetic field changes from 0 to $B = 4\Delta_{SC}$ where $\Delta_{SC} = 0.25meV$. The lines are separated by Zeeman energy of 0.02 meV. (d) DOS for finite quantum wire with Fermi level tuned to the bottom of the (n,m) = (1,0) sub-band. The pair of Andreev states evolve into the Majorana zero modes when the Zeeman energy exceeds the pairing potential in this case.

It has been argued that the zero-bias peak observed in experiments can also be caused by disorder.[58–60] Here we construct a binary disorder model for the chemical potential and pairing potential and use a Gaussian distribution model of the pairing phase disorder. When the Fermi level lies at the lowest sub-band with (n,m) = (1,0), the DOS of the infinite wire with different kinds of disorder is shown in Fig. 5 (a)-(c). To model a charge disorder in the semiconductor we define a spatially varying chemical potential:

$$\mu_i = \mu + \delta\mu_i \tag{13}$$

where $\delta\mu_i$ is a tri-valued variable which is sampled in $(-\delta\mu, 0, \delta\mu)$ randomly for each site i. We find that the

DOS is insensitive to the disorder of chemical potential in the chosen disorder strength $\delta\mu = \Delta_{SC}$ for sub-band with angular $(n, m) = (1, \pm 1)$, as shown in Fig. 5 (a). However, this is not the case for disorder in the phase and amplitude of the superconducting pairing potential. To model the amplitude disorder of pairing potential, we set the amplitude of pairing potential as:

$$|\Delta^i_{SC}| = |\Delta_{SC}| - \delta|\Delta^i_{SC}|, \tag{14}$$

in which $\delta|\Delta^i_{SC}|$ is a binary-valued variable that is sampled randomly in the collection $(0,\delta|\Delta_{SC}|)$. We use this binary model for the assumption that the superconducting metals are not perfectly deposited on the semiconductor quantum wire. For the position with perfect deposited the proximitized superconducting pairing potential is $|\Delta_{SC}|$, while for the position with poorly deposited superconducting metals the pairing potential is $|\Delta_{SC}| - \delta|\Delta^i_{SC}|$. Disorder of the paring potential phase is model as:

$$\Delta^i_{SC} = |\Delta_{SC}|e^{i(\phi_0+\delta\phi_i)}, \tag{15}$$

where ϕ_0 is the average phase of the pairing potential, and the statistics of $\delta\phi_i$ are sampled from a Gaussian function:

$$f(\delta\phi_i) = (1/\sqrt{2\pi}\sigma)e^{-\delta\phi_i^2/2\sigma^2}. \tag{16}$$

We set the variance of the phase to be bounded by $\sigma = \pi/2$, which is the largest phase disorder strength. Disorders in the amplitude and phase of pairing potential lead to substantial changes of the superconductivity gap for the chosen disorder strength as shown in Fig. 5 (b) and (c), decreasing the size of the superconductor gap at the value of disorder strength we used.

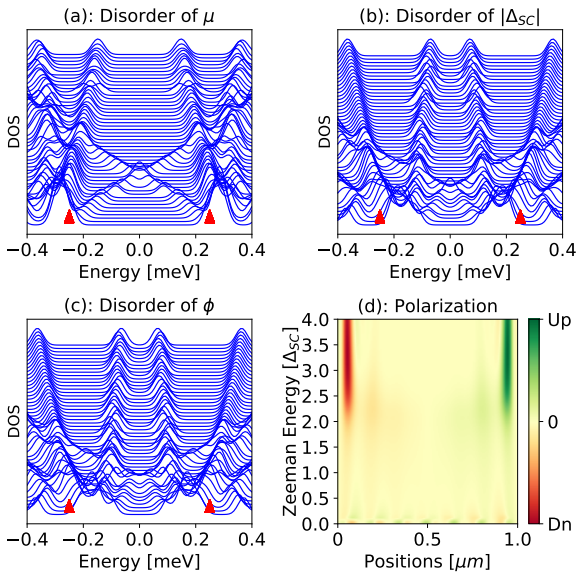

FIG. 5. (Color online). The effect of disorder and magnetic field on Andreev states. (a)-(c) DOS of the infinite wire at the lowest band with different types of disorder: (a) disorder in the chemical potential; (b) pairing amplitude disorder; (c) pairing phase disorder modeled as a normal distribution, with the mean phase as 0 and the variance of the phase as $\pi/2$; (d) The polarization $n_\uparrow - n_\downarrow$ of Andreev states along the quantum wire (here $L = 1$ μm with periodic boundary conditions).

IV. MAJORANA ZERO MODES PROPERTIES

In the previous section, it was shown that disorder in the pairing potential substantial changes the size of the superconductor gap. We now extend this discussion – using the same model and model parameters[14] – to describe a finite quantum wire with a length of 1 μm. Further details of the convergence of energies of Majorana states *vs.* the effective lattice constant is shown in Appendix A.

Fig. 6 (a)-(c) shows the DOS *vs.* the Zeeman energy for disorder in the chemical potential, superconducting order-parameter amplitude, and pairing phase. The superconductivity gap is robust to disorder in the chemical potential but decreases with disorder in the superconducting order-parameter amplitude and phase at the chosen disorder strength for the (n,m) = (1,±1) sub-band.

This sensitivity to magnetic fields found in the finite system is not only a symptom of disorder. The Majorana modes in the finite system are more sensitive to magnetic field than the Andreev states seen in the infinite system even in the absence of disorder. The polarization of the two states closest to zero energy, calculated as $n_\uparrow - n_\downarrow$ as in Fig. 6(d), shows that the Zeeman energy needed to polarize the Majorana modes is the size of the pairing potential. This can be compared to Fig. 5(d) showing the same quantity in the infinite wire where the Zeeman energy required to polarize these states is a factor of ≈ 2 times the pairing potential. With these results we find that the Andreev bound states in the infinite wire require a larger Zeeman energy to polarize than the Majorana zero-modes even in the absence of disorder.

For finite quantum wires, the Majorana end modes fuse into Fermionic excitations at a finite energy ϵ_0[65]. To study the disorder effect in the general case, we have plotted the energies of Fermionic excitations ($2\epsilon_0 = E^0_+ - E^0_-$) combined by two Majorana end modes (or Andreev modes if the quantum wire is in the trivial superconducting phase) and the lowest-lying bulk energy level ($2\epsilon_1 = E^1_+ - E^1_-$) with varied disorder strengths. This is shown in Fig. 7 (a)-(c) for (n,m) = (1,0) sub-band and in (d)-(f) for (n,m) = (1,±1) sub-bands. The energies of Fermionic excitations are shown in solid curves, while the lowest-lying bulk energy levels are labeled with dotted curves, and different colors represent different Zeeman energies. For (n,m) = (1,0) sub-bands, the energies of Fermionic excitations are insensitive to chemical potential disorder up to the strength of $\delta\mu \approx \Delta_{SC}$. Similar dependence happens for the (n,m) = (1,±1) sub-band. The critical disorder strength, which depends on superconducting coherence length and topological coherence

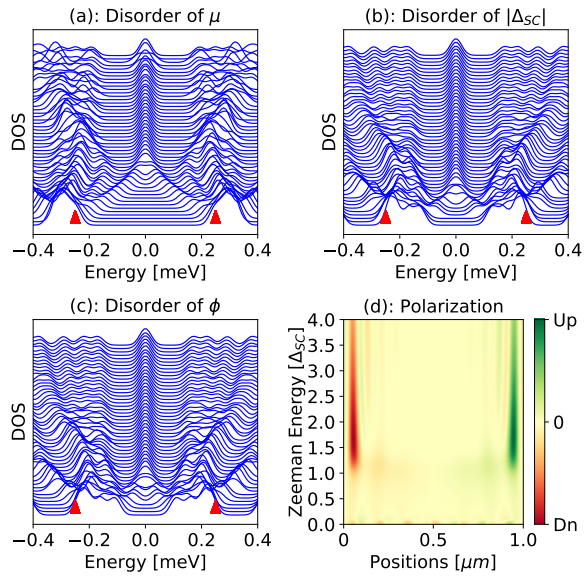

FIG. 6. (Color online). DOS at the lowest sub-band with quantum number (n,m) = (1,±1) in the finite quantum wire. The magnetic field changes from 0 at the bottom of the plots in increments of 0.02 meV up to $B = 4\Delta_{SC}$ at the top of the plots. Again, the pairing potential is $\Delta_{SC} = 0.25meV$. (a) Disorder in the chemical potential; (b) Disorder of pairing amplitude; (c) Disorder of pairing phase; (d) Polarization of Majorana zero modes along the quantum wire (with $L = 1\ \mu m$).

length[65–68], is thus around $\delta\mu \approx \Delta_{SC}$ and varies with the Zeeman energy.

However, there is a different dependence on disorder strength of pairing potential for (n,m) = (1,0) and (n,m) = (1,±1) sub-bands. In the range of disorder strength $\delta|\Delta_{SC}| < 0.5\Delta_{SC}$ and $\sigma < \pi/4$ for pairing potential amplitude and phase disorder case, energies of Fermionic excitations for (n,m) = (1,0) sub-band have a monotonically decreasing dependence on the disorder strength when Zeeman energies are small. Beyond this disorder strength, the energies of Fermionic excitations and lowest-lying bulk energy levels increase. Note that the disorder of pairing potential amplitude and phase have similar dependence on the strength. For (n,m) = (1,±1) sub-bands, however, the energies of Fermionic excitations always decrease in the range of disorder strengths we calculates.

In Fig. 8 we show the energies of Fermionic excitations (solid lines) and lowest-lying bulk energy level (dashed lines) *vs.* Zeeman splitting with varied disorder strengths. In the plots x-axis is the Zeeman splitting, and different disorder strength is represented by different colors. Fig. 8 (a)-(c) are the plots for sub-bands (n,m) = (1,0), while Fig. 8 (d)-(f) are for the sub-bands (n,m) = (1,±1). Solid and dashed lines with the same color label the same disorder strength. In the absence of magnetic field, the pairing potential behaviors insensitive to the strength of chemical potential disorder, however, the disorder of pairing potential and phase do reduce the superconducting gap. When the magnetic field is applied, the critical magnetic field for Fermionic excitations gap does not appear significant changes until the strength of disorder exceeds the critical value discussed above.

In tunneling experiments on proximitized quantum wire systems, the local density of states at the end of the quantum wire is probed. The DOS at the edge of the superconducting gap is found to be larger than the zero-biased peak associated with Majorana modes. We can probe this feature in our model by calculating the projected DOS for different length scales measured from the end of the wire. Fig. 9 (a) and (b) shows the projected DOS parameterized by the Zeeman energy for states projected within 50 nm, and 250 nm from the end of the wire (the length of the wire in this simulation is 1 μm). In this way we can compare states at the end of the wire with the bulk system. While we find the DOS near the edge of the gap is small when we focus on the end of the wire (Fig. 9 (a)), this becomes comparable with the zero-bias peak when we include more bulk states (Fig. 9 (b)). The size of the DOS at the superconducting gap energy relative to the zero-bias peak found in experiments, can thus not be accounted for by this model.

V. DISCUSSION

In this paper, we have studied the properties of cylindrical semiconducting quantum wires proximity coupled to a superconductor. Topological states occur in the presence of an external magnetic field for Fermi levels just above the population thresholds of all angular momentum $m = 0$ quasi-one-dimensional sub-bands. Majorana zero modes are localized near wire-ends at $m = 0$ sub-band population thresholds. In contrast, pairs of localized Majorana-like states appear at each end near the population thresholds of degenerated sub-bands when magnetic orbital effects are negligible. This states can give rise to zero-bias anomalies in transport. Furthermore, we studied the influence of disorder of chemical potential and pairing potential amplitude with a binary model. However, this binary model does give a similar dependence of superconducting gap on disorder compared with the disorder based on Gaussian distribution[69] in one-dimensional lattice model.

The DOS measured in experiments strongly depends on not only the Majorana zero modes spectrum, but also the superconducting element which donates its superconductivity to the semiconductor quantum wire. We clarify this point by estimating the semiconductor and metal (superconductor) electron density for direct comparison (See Appendix C for details). We find that the number of electrons in the metal/superconductor N_{sc} greatly outnumbers the number of electrons in the semiconductor N_{qw} ($N_{sc} >> N_{qw}$), with their ratio ranging from $\sim 10^3$ to $\sim 10^5$ depending on the specific materials. Summarized in Table I, which includes semiconductor quantum

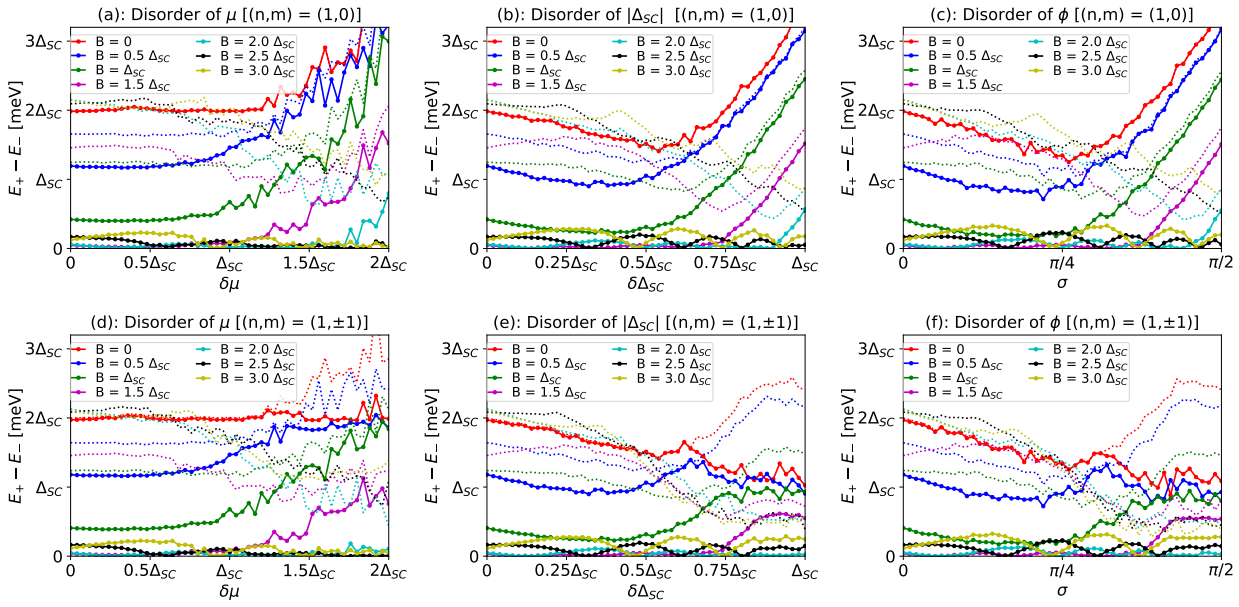

FIG. 7. (Color online). Dependence on disorder strength for energies of Fermionic excitations combined by two Majorana end modes(or Andreev modes) $2\epsilon_0 = E_+^0 - E_-^0$ (solid curves), and for lowest-lying bulk energy level $2\epsilon_1 = E_+^1 - E_-^1$ (dotted curves). In the plots x-axis is the disorder strength, different color represent different Zeeman energy. For solid and dotted lines with the same color, they label the same Zeeman energy. (a)-(c) are the plots for sub-bands (n,m) = (1,0), while (d)-(f) are for the sub-bands (n,m) = (1,±1).

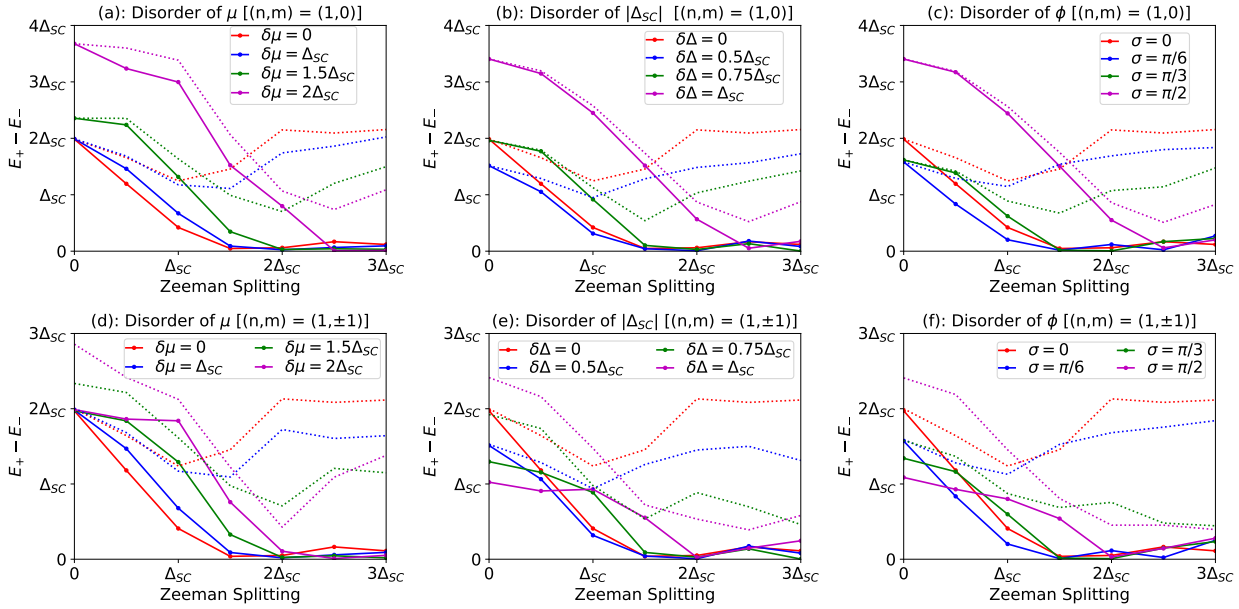

FIG. 8. (Color online). Energis of Fermionic excitations $2\epsilon_0 = E_+^0 - E_-^0$ (solid curves) and lowest-lying bulk energy level $2\epsilon_1 = E_+^1 - E_-^1$ (dotted curves) *vs.* Zeeman splitting with various disorder strength. In the plots x axis is the Zeeman splitting, different color represent different disorder strength. (a)-(c) are the plots for sub-bands (n,m) = (1,0), while (d)-(f) are for the sub-bands (n,m) = (1,±1). For solid and dashed lines with the same color, they label the same disorder strength.

wires with various cross sections including cylindrical and hexagonal quantum wires, are the estimates of the electron count. The number of electrons in the superconducting metal is many orders of magnitude larger than the number of electrons in the semiconductor quantum wire.

This shows that electrons in the superconducting metals will play an important role in understanding measurements of Majorana zero-modes in proximatized quantum wires, an indirect evidence is that the superconducting

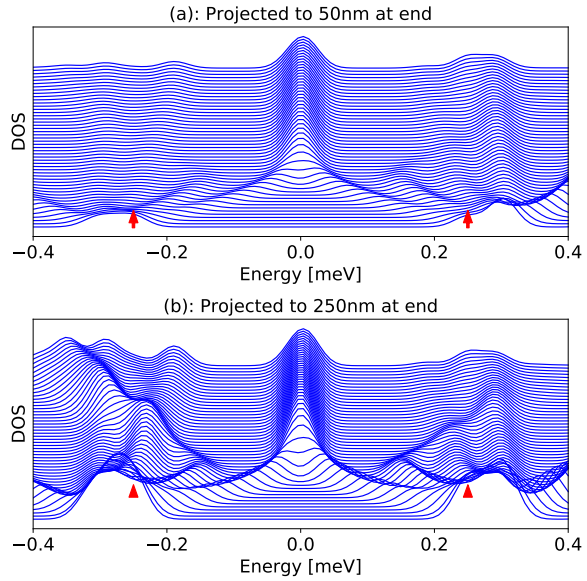

FIG. 9. (Color online). Projected DOS at the end of the quantum wire. (a) is the results of DOS projected at the end within $50nm$ and (b) is the results of DOS projected at the end within $250nm$.

TABLE I. Extracted experimental parameters. The ratio of the superconducting pairing potential Δ to the spin-orbit energy E_{so}, the number of electrons in the quantum wire N_{qw}, and the ratio of the number of electrons in the superconductor N_{sc} to the number of electrons in the quantum wire.

Materials	Δ/E_{so}	N_{qw}	N_{sc}/N_{qw}
InSb/Nb[14]	0.8	5.0	2.0×10^5
InSb/Nb[19]	0.6	1.4	2.3×10^4
InAs/Al[16]	0.8	0.4	1.3×10^4
Nb/InSb/Nb[15]	0.3	3.0	1.4×10^5
InSb/NbTiN[17]	1.4	0.6	2.3×10^5
InAs/NbN[18]	16.5	1.9	4.8×10^4
InAs/Al[20,21]	2.1	0.6-2.5	9.3×10^2

gap measured in semiconductor quantum wires (typically $0.15-0.2$ meV for Aluminum for example) is very close to the bulk superconducting gap (which is ~ 0.2 meV, a summary of this parameters can be found in ref. 7). A complete model that includes both electrons in semiconductor quantum wires and superconducting metal explicitly[9] is thus necessary.

The present proximitized semiconductor quantum wire based Majorana systems may be in fact treated as a superconducting metal perturbed by magnetic field and spin-orbit interaction proximitized by semiconductor quantum wires, the main contribution to the tunneling DOS comes from the electrons in superconducting metal instead of the semiconductor quantum wire. Ultrathin film metals with strong spin-orbit coupling[70] are thus a prospective platform to realize topological superconductors if the g-factor is large enough and effective tools are found to tune the Fermi level.

VI. ACKNOWLEDGEMENTS

This work was financially supported by Welch Foundation under grant Welch F-1473 and by Army Research Office under Grant Number W911NF-16-1-0472.

Appendix A: Convergence with effective lattice constant

For quantum wires with infinite length (that with periodic boundary condition), the energies of Andreev states *vs.* effective lattice constant b are shown in Fig. 10, in which we may see that the energies are converged at the effective lattice constant of $b\approx 100$ nm. Note that in Fig. 10(a) the two modes are labeled with green dotted solid lines, while in Fig. 10(b) there are four modes, which are labeled with blue dots and green solid lines. To get reliable results $b=5$ nm is used in our calculations.

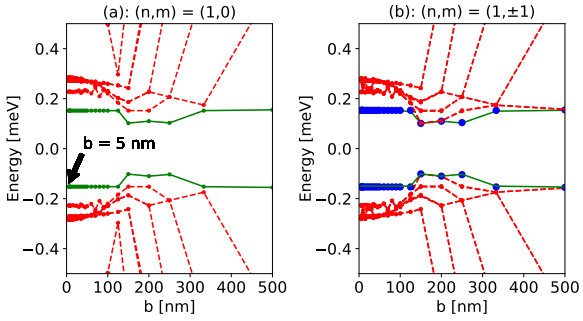

FIG. 10. (Color online). Selected eigenenergies close to the chemical potential *vs.* the effective lattice constant b for quantum wires with infinite length. The periodic quantum wire length is set to 1 μm. In the plots the energies of Andreev states are already converged at the effective lattice constant of $b\approx 100$ nm. The bulk states (red dashed lines), the two Andreev states (green dotted lines) in (a) and the four Andreev states (green lines and blue dots) in (b) are well converged at $b=5$ nm, the value used in this work.

The convergence of energies of Majorana states *vs.* the effective lattice constant is shown in Fig. 11(a) where the two modes are labeled with green dotted solid lines, and in Fig. 11(b) where four Majorana modes are shown and labeled with blue dots and green solid lines.

Appendix B: Radial and angular quantum numbers

Although $-i\sin\varphi\frac{\partial}{\partial r}$ or $-i\frac{\cos\varphi}{r}\frac{\partial}{\partial\varphi}$ is not Hermitian, the sum of them is in fact Hermitian as we show below. In the cylindrical coordinate, we have:

$$x=r\cos\varphi,\qquad y=r\sin\varphi, \tag{B1}$$

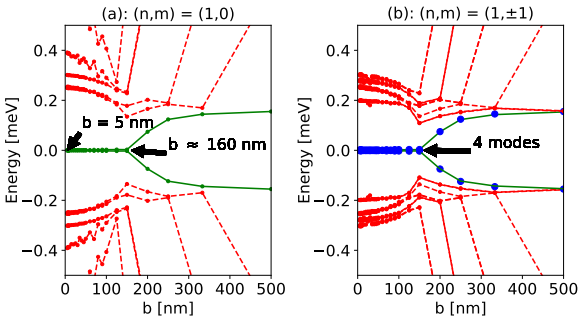

FIG. 11. (Color online). Selected eigen-energies close to the chemical potential *vs.* the effective lattice constant b for quantum wires with finite length. The quantum wire length is set to 1 μm. The energies of Majorana states are converged at an effective lattice constant of $b \approx 160$ nm. The bulk states (red dashed lines), the two Majorana states (green dotted lines) in (a) and the four Majorana states (green lines and blue dots) in (b) are well converged at $b = 5$ nm, the value used in this work.

with $r = \sqrt{x^2 + y^2}$. We may separate the Rashba term into two parts:

$$\frac{\partial}{\partial y} = -i(\sin\varphi \frac{\partial}{\partial r} + \frac{\cos\varphi}{r}\frac{\partial}{\partial \varphi}) \equiv \hat{p_r'} + \hat{p_\varphi'}, \tag{B2}$$

that is composed with a radial momentum operator $\hat{p_r'}$ and a angular momentum operator $\hat{p_\varphi'}$. For radial momentum operator, the matrix elements are:

$$\begin{aligned}\langle \hat{p_r'} \rangle_{ij} &= -i \int_0^{2\pi} d\varphi \sin\varphi \int_0^{\infty} r dr \Psi_i^*(r,\varphi) \frac{\partial \Psi_j(r,\varphi)}{\partial r} \\ &= \langle \hat{p_r'} \rangle_{ji}^* + i \int_0^{2\pi} d\varphi \sin\varphi \int_0^{\infty} dr \Psi_i^*(r,\varphi)\Psi_j(r,\varphi).\end{aligned} \tag{B3}$$

For angular momentum operator,

$$\begin{aligned}\langle \hat{p_\varphi'} \rangle_{ij} &= -i \int_0^{\infty} r dr \int_0^{2\pi} d\varphi \frac{\cos\varphi}{r} \Psi_i^*(r,\varphi) \frac{\partial \Psi_j(r,\varphi)}{\partial d\varphi} \\ &= \langle \hat{p_\varphi'} \rangle^* - i \int_0^{\infty} dr \int_0^{2\pi} d\varphi \sin\varphi \Psi^*(r,\varphi)\Psi(r,\varphi).\end{aligned} \tag{B4}$$

Note that in above equations the non-Hermitian parts of radial and angular momentum operators cancel, We thus have:

$$\langle \hat{p_r'} + \hat{p_\varphi'} \rangle_{ij} = \langle \hat{p_r'} + \hat{p_\varphi'} \rangle_{ji}^*. \tag{B5}$$

Appendix C: Estimation of experimental parameters

To estimate the electrons involved in Majorana zero modes in semiconductor quantum wire, we consider the active sub-band and model it with the following quasi-one-dimensional Hamiltonian:

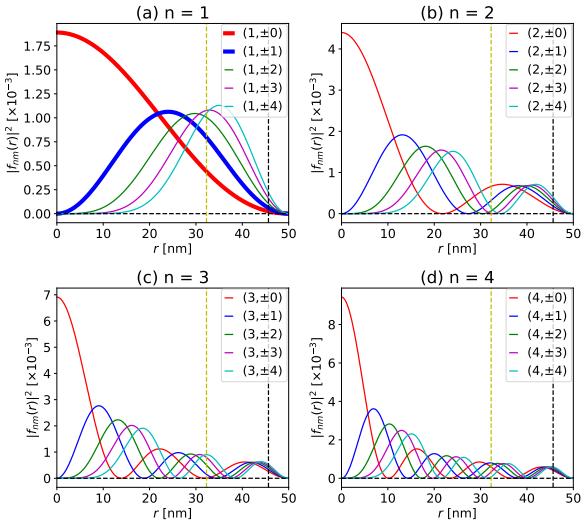

FIG. 12. Radial distribution of wavefunctions for different quantum numbers (n.m). The thickened red and blue lines in (a) are the two subbands whose results are shown in our manuscript. The yellow and black dashed vertical line labels the magnetic length corresponding to the magnetic field of 0.3 T and 0.6 T, the related Zeeman energy is around $2\Delta_{SC}$ and $4\Delta_{SC}$.

$$H_k = \frac{\hbar^2}{2m^*}k^2 + \alpha k \sigma_y \tag{C1}$$

where $\hbar$ is the reduced Plank constant, m^* is the effective mass of electrons in semiconductor, α is the Rashba coupling. The band energy can be solved to be:

$$E_k = \frac{\hbar^2}{2m^*}k^2 \pm \alpha k. \tag{C2}$$

To estimate the number of electron in the semiconductor quantum wires N_{qw}, we take advantage of the quasi-1D nature of the wires and find $N_{qw} = \frac{k_{so} \cdot L}{\pi}$(see Table I). Here $k_{so} = \frac{2\alpha m^*}{\hbar^2}$ is the spin-orbit wave vector and L is the length of quantum wire. This assumes that the chemical potential has been tuned to E_{so} by the gate voltage. The spin-orbit wave vector and spin-orbit energy $E_{so} = \frac{\alpha^2 m^*}{2\hbar^2} = \frac{\alpha}{4}k_{so}$ are estimated from the extracted experimental effective electron mass m^* and Rashba coupling α. The estimation of the experimental parameters in semiconductor quantum wire are shown in Table II.

Via proximity effect, the Cooper pairs tunnel into the quantum wire, the DOS in Aluminum is

$$D(E_F) = \frac{m^*}{\pi^2\hbar^3}\sqrt{2m^*E_F} = \frac{2m^*}{\hbar^2 k_F^2}\frac{\hbar^2 k_F^2}{2\pi^2}\sqrt{\frac{2m^*}{\hbar^2}E_F} \tag{C3}$$

since $E_F = \frac{\hbar^2 k_F^2}{2m^*}$, then

$$D(E_F) = \frac{1}{E_F}\frac{k_F^2}{2\pi^2}\sqrt{\frac{1}{E_F}k_F^2 E_F} = \frac{1}{E_F}\frac{k_F^3}{2\pi^2} \tag{C4}$$

TABLE II. Summary of parameters of semiconductor quantum wires.

Materials	Geometry	L[nm]	$\alpha[eVnm]$	$m^*[m_e]$	$k_{so}[nm^{-1}]$	$\lambda_F[nm]$	$r_{ee}[nm]$	$E_{so}[meV]$	N_{qw}
InSb/Nb[14]	Cir	~ 2000	0.02	0.015	0.0079	127	399	0.315	5
InSb/Nb[19]	Ret	~ 600	0.019	0.015	0.0075	134	420	0.284	1.4
InAs/Al[16]	Cir	~ 150	0.0113	0.03	0.0089	112	353	0.201	0.4
Nb/InSb/Nb[15]	Cir	$\sim 740(680)$	0.032	0.015	0.0126	79	250	0.806	3(2.7)
InSb/NbTiN[17]	Cir	~ 250	0.02	0.015	0.0079	127	399	0.315	0.6
InAs/NbN[18]	Cir	~ 1000	0.01	0.023	0.006	166	520	0.121	1.9
InAs/Al[20,21]	Hex	$330-1500$	0.008	0.025	0.0052	190	598	0.084	0.6-2.5

while the density of free electron in 3D system is $n = \frac{2\cdot 4\pi k_F^3}{(2\pi)^3} \rightarrow k_F^3 = 3\pi^2 n$, then the DOS is

$$D(E_F) = \frac{3n}{2E_F} \tag{C5}$$

To calculate the number density of free electrons (n):

$$n = z\frac{N_A}{V_A} \tag{C6}$$

where z is the valency,N_A is the Avogadros constant,V_A is the molar volume.To calculate the molar volume:

$$V_A = \frac{M_r \times 10^{-3}}{\rho} \tag{C7}$$

where M_r is the relative atomic mass (the 10^{-3} is to convert M_r from grams to kg),ρ is the density. We then get

$$n = \frac{z\rho N_A}{M_r \times 10^{-3}} \tag{C8}$$

For Aluminum $z = 3$ and $M_r = 27$, while for Niobium, $z = 5$ and $M_r = 93$, and the Avogadro constant is 6.02×10^{23}, then $n = 1.8 \times 10^{29} m^{-3}$ for Aluminum and $n = 2.8 \times 10^{29} m^{-3}$ for Niobium.

The number of electron in the superconducting metal is estimated by:

$$N_{so} = D(E_F) \cdot E_{so} \cdot V_{sc} = \frac{3n}{2}\frac{E_{so}}{E_F} \cdot V_{sc}, \tag{C9}$$

where V_{sc} is the volume of the superconducting shell, this expression for N_{sc} assumes that the DOS is constant on the scale of E_{so} and that only electrons near E_{so} contribute, the corresponding parameters estimated from experiments are shown in Tabel III.

TABLE III. Summary of parameters of superconducting metals.

Materials	$V_{SC}[10^6 nm^3]$	$\Delta[meV]$	$N_{sc}[10^4]$
InSb/Nb[14]	40	0.25	99.46
InSb/Nb[19]	1.44	0.18	3.23
InAs/Al[16]	1.18	0.15	0.55
Nb/InSb/Nb[15]	6.65(6.11)	0.25	42.33(38.89)
InSb/NbTiN[17]	5.89	0.45	14.65
InAs/NbN[18]	9.64	2	9.19
InAs/Al[20,21]	0.264-1.2	0.18	0.05-0.23

[1] A. Y. Kitaev, Physics-Uspekhi **44**, 131 (2001).
[2] E. Majorana, Il Nuovo Cimento **14**, 171 (1937).
[3] C. Nayak, S. H. Simon, A. Stern, M. Freedman, and S. Das Sarma, Rev. Mod. Phys. **80**, 1083 (2008).
[4] J. Alicea, Reports on Progress in Physics **75**, 076501 (2012).
[5] C. Beenakker, Annu. Rev. Condens. Matter Phys. **4**, 113 (2013).
[6] S. R. Elliott and M. Franz, Rev. Mod. Phys. **87**, 137 (2015).
[7] R. M. Lutchyn, E. P. A. M. Bakkers, L. P. Kouwenhoven, P. Krogstrup, C. M. Marcus, and Y. Oreg, Nature Reviews Materials **3**, 5268 (2018).
[8] M. Leijnse and K. Flensberg, Semiconductor Science and Technology **27**, 124003 (2012).
[9] T. D. Stanescu and S. Tewari, Journal of Physics: Condensed Matter **25**, 233201 (2013).
[10] N. Read and D. Green, Phys. Rev. B **61**, 10267 (2000).
[11] D. A. Ivanov, Phys. Rev. Lett. **86**, 268 (2001).
[12] R. M. Lutchyn, J. D. Sau, and S. Das Sarma, Phys. Rev. Lett. **105**, 077001 (2010).
[13] Y. Oreg, G. Refael, and F. von Oppen, Phys. Rev. Lett. **105**, 177002 (2010).
[14] V. Mourik, K. Zuo, S. Frolov, S. Plissard, E. Bakkers, and L. Kouwenhoven, Science **336**, 1003 (2012).
[15] M. Deng, C. Yu, G. Huang, M. Larsson, P. Caroff, and H. Xu, Nano letters **12**, 6414 (2012).
[16] A. Das, Y. Ronen, Y. Most, Y. Oreg, M. Heiblum, and H. Shtrikman, Nature Physics **8**, 887 (2012).
[17] H. O. H. Churchill, V. Fatemi, K. Grove-Rasmussen, M. T. Deng, P. Caroff, H. Q. Xu, and C. M. Marcus, Phys. Rev.

B **87**, 241401 (2013).
[18] A. D. K. Finck, D. J. Van Harlingen, P. K. Mohseni, K. Jung, and X. Li, Phys. Rev. Lett. **110**, 126406 (2013).
[19] L. P. Rokhinson, X. Liu, and J. K. Furdyna, Nature Physics **8**, 795 (2012).
[20] S. M. Albrecht, A. Higginbotham, M. Madsen, F. Kuemmeth, T. S. Jespersen, J. Nygård, P. Krogstrup, and C. Marcus, Nature **531**, 206 (2016).
[21] M. T. Deng, S. Vaitiekenas, E. B. Hansen, J. Danon, M. Leijnse, K. Flensberg, J. Nygård, P. Krogstrup, and C. M. Marcus, Science **354**, 1557 (2016).
[22] Ö. Gül, H. Zhang, J. D. Bommer, M. W. de Moor, D. Car, S. R. Plissard, E. P. Bakkers, A. Geresdi, K. Watanabe, T. Taniguchi, *et al.*, Nature nanotechnology **13**, 192 (2018).
[23] J. Chen, P. Yu, J. Stenger, M. Hocevar, D. Car, S. R. Plissard, E. P. A. M. Bakkers, T. D. Stanescu, and S. M. Frolov, Science Advances **3** (2017), 10.1126/sciadv.1701476, http://advances.sciencemag.org/content/3/9/e1701476.full.pdf.
[24] H. J. Suominen, M. Kjaergaard, A. R. Hamilton, J. Shabani, C. J. Palmstrøm, C. M. Marcus, and F. Nichele, Phys. Rev. Lett. **119**, 176805 (2017).
[25] F. Nichele, A. C. C. Drachmann, A. M. Whiticar, E. C. T. O'Farrell, H. J. Suominen, A. Fornieri, T. Wang, G. C. Gardner, C. Thomas, A. T. Hatke, P. Krogstrup, M. J. Manfra, K. Flensberg, and C. M. Marcus, Phys. Rev. Lett. **119**, 136803 (2017).
[26] J. E. Sestoft, T. Kanne, A. N. Gejl, M. von Soosten, J. S. Yodh, D. Sherman, B. Tarasinski, M. Wimmer, E. Johnson, M. Deng, J. Nygård, T. S. Jespersen, C. M. Marcus, and P. Krogstrup, Phys. Rev. Materials **2**, 044202 (2018).
[27] M.-T. Deng, S. Vaitiekėnas, E. Prada, P. San-Jose, J. Nygård, P. Krogstrup, R. Aguado, and C. M. Marcus, Phys. Rev. B **98**, 085125 (2018).
[28] S. Vaitieknas, G. W. Winkler, B. van Heck, T. Karzig, M.-T. Deng, K. Flensberg, L. I. Glazman, C. Nayak, P. Krogstrup, R. M. Lutchyn, and et al., Science **367**, eaav3392 (2020).
[29] S.-B. Zhang, A. Calzona, and B. Trauzettel, "All-electrically tunable networks of majorana bound states," (2020), arXiv:2003.04053 [cond-mat.supr-con].
[30] X. P. Zhang, V. N. Golovach, F. Giazotto, and F. S. Bergeret, Phys. Rev. B **101**, 180502 (2020).
[31] X.-Q. Li and L. Xu, Phys. Rev. B **101**, 205401 (2020).
[32] J. Ekström, P. Recher, and T. L. Schmidt, Phys. Rev. B **101**, 195420 (2020).
[33] J. S. Lee, B. Shojaei, M. Pendharkar, A. P. McFadden, Y. Kim, H. J. Suominen, M. Kjaergaard, F. Nichele, H. Zhang, C. M. Marcus, and et al., Nano Letters **19**, 30833090 (2019).
[34] L. S. Ricco, M. de Souza, M. S. Figueira, I. A. Shelykh, and A. C. Seridonio, Phys. Rev. B **99**, 155159 (2019).
[35] G. W. Winkler, A. E. Antipov, B. van Heck, A. A. Soluyanov, L. I. Glazman, M. Wimmer, and R. M. Lutchyn, Phys. Rev. B **99**, 245408 (2019).
[36] A. E. Antipov, A. Bargerbos, G. W. Winkler, B. Bauer, E. Rossi, and R. M. Lutchyn, Phys. Rev. X **8**, 031041 (2018).
[37] C. Chan, L. Zhang, T. F. J. Poon, Y.-P. He, Y.-Q. Wang, and X.-J. Liu, Phys. Rev. Lett. **119**, 047001 (2017).
[38] M. Kjærgaard, F. Nichele, H. J. Suominen, M. Nowak, M. Wimmer, A. Akhmerov, J. Folk, K. Flensberg, J. Shabani, w. C. Palmstrøm, *et al.*, Nature communications **7**, 12841 (2016).
[39] F. Nichele, A. C. C. Drachmann, A. M. Whiticar, E. C. T. O'Farrell, H. J. Suominen, A. Fornieri, T. Wang, G. C. Gardner, C. Thomas, A. T. Hatke, P. Krogstrup, M. J. Manfra, K. Flensberg, and C. M. Marcus, Phys. Rev. Lett. **119**, 136803 (2017).
[40] C. Bøttcher, F. Nichele, M. Kjaergaard, H. Suominen, J. Shabani, C. Palmstrøm, and C. Marcus, Nature Physics **14**, 1138 (2018).
[41] F. Pientka, A. Keselman, E. Berg, A. Yacoby, A. Stern, and B. I. Halperin, Phys. Rev. X **7**, 021032 (2017).
[42] J. Shabani, M. Kjaergaard, H. J. Suominen, Y. Kim, F. Nichele, K. Pakrouski, T. Stankevic, R. M. Lutchyn, P. Krogstrup, R. Feidenhans'l, S. Kraemer, C. Nayak, M. Troyer, C. M. Marcus, and C. J. Palmstrøm, Phys. Rev. B **93**, 155402 (2016).
[43] M. Hell, M. Leijnse, and K. Flensberg, Phys. Rev. Lett. **118**, 107701 (2017).
[44] H. J. Suominen, M. Kjaergaard, A. R. Hamilton, J. Shabani, C. J. Palmstrøm, C. M. Marcus, and F. Nichele, Phys. Rev. Lett. **119**, 176805 (2017).
[45] S. Nadj-Perge, I. K. Drozdov, J. Li, H. Chen, S. Jeon, J. Seo, A. H. MacDonald, B. A. Bernevig, and A. Yazdani, Science **346**, 602 (2014).
[46] R. Pawlak, M. Kisiel, J. Klinovaja, T. Meier, S. Kawai, T. Glatzel, D. Loss, and E. Meyer, npj Quantum Information **2**, 16035 (2016), arXiv:1505.06078 [physics.atm-clus].
[47] M. Ruby, F. Pientka, Y. Peng, F. von Oppen, B. W. Heinrich, and K. J. Franke, Phys. Rev. Lett. **115**, 197204 (2015).
[48] M.-X. Wang, C. Liu, J.-P. Xu, F. Yang, L. Miao, M.-Y. Yao, C. L. Gao, C. Shen, X. Ma, X. Chen, Z.-A. Xu, Y. Liu, S.-C. Zhang, D. Qian, J.-F. Jia, and Q.-K. Xue, Science **336**, 52 (2012), http://science.sciencemag.org/content/336/6077/52.full.pdf.
[49] Q. L. He, L. Pan, A. L. Stern, E. C. Burks, X. Che, G. Yin, J. Wang, B. Lian, Q. Zhou, E. S. Choi, K. Murata, X. Kou, Z. Chen, T. Nie, Q. Shao, Y. Fan, S.-C. Zhang, K. Liu, J. Xia, and K. L. Wang, SCIENCE **357**, 294 (2017).
[50] D. Wang, L. Kong, P. Fan, H. Chen, S. Zhu, W. Liu, L. Cao, Y. Sun, S. Du, J. Schneeloch, R. Zhong, G. Gu, L. Fu, H. Ding, and H.-J. Gao, Science **362**, 333 (2018), http://science.sciencemag.org/content/362/6412/333.full.pdf.
[51] H. Ren, F. Pientka, S. Hart, A. T. Pierce, M. Kosowsky, L. Lunczer, R. Schlereth, B. Scharf, E. M. Hankiewicz, L. W. Molenkamp, *et al.*, Nature **569**, 93 (2019).
[52] S. Hart, H. Ren, M. Kosowsky, G. Ben-Shach, P. Leubner, C. Brüne, H. Buhmann, L. W. Molenkamp, B. I. Halperin, and A. Yacoby, Nature Physics **13**, 87 (2017).
[53] F. Wilczek, Nature Physics **5**, 614 (2009).
[54] A. Stern, Nature **464**, 187 (2010).
[55] M. Franz, Physics **3**, 24 (2010).
[56] C. Nayak, Nature **464**, 693 (2010).
[57] C.-X. Liu, J. D. Sau, T. D. Stanescu, and S. Das Sarma, Phys. Rev. B **96**, 075161 (2017).
[58] D. Bagrets and A. Altland, Phys. Rev. Lett. **109**, 227005 (2012).
[59] J. Liu, A. C. Potter, K. T. Law, and P. A. Lee, Phys. Rev. Lett. **109**, 267002 (2012).
[60] D. Pikulin, J. Dahlhaus, M. Wimmer, H. Schomerus, and C. Beenakker, New Journal of Physics **14**, 125011 (2012).
[61] E. J. H. Lee, X. Jiang, R. Aguado, G. Katsaros, C. M. Lieber, and S. De Franceschi, Phys. Rev. Lett. **109**, 186802

(2012).
[62] L. Villegas-Lelovsky, C. Trallero-Giner, M. Rebello Sousa Dias, V. Lopez-Richard, and G. E. Marques, Phys. Rev. B **79**, 155306 (2009).
[63] J. Soo Lim, R. Lopez, and L. Serra, EPL (Europhysics Letters) **103**, 37004 (2013).
[64] G. W. Winkler, D. Varjas, R. Skolasinski, A. A. Soluyanov, M. Troyer, and M. Wimmer, Phys. Rev. Lett. **119**, 037701 (2017).
[65] P. W. Brouwer, M. Duckheim, A. Romito, and F. von Oppen, Phys. Rev. Lett. **107**, 196804 (2011).
[66] O. Motrunich, K. Damle, and D. A. Huse, Phys. Rev. B **63**, 224204 (2001).
[67] I. A. Gruzberg, N. Read, and S. Vishveshwara, Phys. Rev. B **71**, 245124 (2005).
[68] P. W. Brouwer, M. Duckheim, A. Romito, and F. von Oppen, Phys. Rev. B **84**, 144526 (2011).
[69] S. Takei, B. M. Fregoso, H.-Y. Hui, A. M. Lobos, and S. Das Sarma, Phys. Rev. Lett. **110**, 186803 (2013).
[70] C. Lei, H. Chen, and A. H. MacDonald, Phys. Rev. Lett. **121**, 227701 (2018).